Quantifying the Spin-Wave Asymmetry in Single and Double Rectangular $Ni_{80}Fe_{20}$ Microstrips by TR-STXM, FMR, and Micromagnetic Simulations

Santa Pile[1], Andreas Ney[1], Kilian Lenz[2], Ryszard Narkowicz[2], Jürgen Lindner[2], Sebastian Wintz[3,4], Johannes Förster[3], Sina Mayr[5,6], and Markus Weigand[4]

[1]Solid State Physics Division, Institute of Semiconductor and Solid State Physics, Johannes Kepler University Linz, 4040 Linz, Austria
[2]Helmholtz-Zentrum Dresden-Rossendorf, Institute of Ion Beam Physics and Materials Research, 01328 Dresden, Germany
[3]Max Planck Institute for Intelligent Systems, 70569 Stuttgart, Germany
[4]Helmholtz-Zentrum Berlin für Materialien und Energie, 12489 Berlin, Germany
[5]Paul Scherrer Institute, 5232 Villigen, Switzerland
[6]Laboratory for Mesoscopic Systems, Department of Materials, ETH Zürich, 8093 Zürich, Switzerland

The asymmetry of spin-wave (SW) patterns in confined rectangular $Ni_{80}Fe_{20}$ microstrips, both in single- and double-strip geometries, is quantified. The results of time-resolved scanning transmission X-ray microscopy (TR-STXM) and micromagnetic simulations are compared. For the TR-STXM measurements and the corresponding simulations, the excitation was a uniform microwave (MW) field with a fixed frequency of 9.43 GHz, while the external static magnetic field was swept. In the easy axis orientation of the analyzed microstrip, the results show a higher asymmetry for the double microstrip design, indicating an influence of the additional microstrip placed in close proximity to the analyzed one.

***Index Terms*— Ferromagnetic resonance (FMR), magnonics, micromagnetics, mumax3, spin waves (SWs), SW imaging, SW symmetry, time-resolved scanning transmission X-ray microscopy (TR-STXM).**

I. Introduction

SPIN-WAVE (SW) dynamics research in confined rectangular nano- and microstructures is important for the rapidly growing fields of magnonics and spintronics [1], [2], [3], [4], [5]. It was shown that the SW behavior can be affected by different factors, for example, temperature [6] or the design of microstructures [7], [8], which in turn can be used as a manipulating mechanism. In the present work, the focus is put on the fundamental understanding of the SW behavior in confined rectangular structures under uniform excitation, depending on the relative positioning of two microstrips [9].

The development of planar microresonators/microantennas containing a microloop (see an example in Fig. 1) allows for focusing microwave (MW) magnetic fields such that they are mainly uniform in the region where the microstructure is located [10]. At the same time, they offer a very high sensitivity for ferromagnetic resonance (FMR) spectroscopy of small structures in comparison to cavity resonators due to an increased filling factor [11]. Time-resolved scanning transmission X-ray microscopy (TR-STXM) [12], [13] in combination with planar microresonators enables direct, time-dependent imaging of the spatial distribution of the precessing magnetization across nanometer-thin microstrips during FMR excitation in the GHz frequency range with elemental selectivity [9], [14].

In general, the confinement of magnetic structures leads to the quantization of SW k-vectors along the axis of confinement [15]. The SW spectrum of a uniformly magnetized ellipsoidal magnetic element can be calculated analytically [16], [17]. However, in most of the cases the magnetic elements used in or considered for applications have a non-ellipsoidal shape. The demagnetizing field and, therefore, the internal magnetic field in rectangular microstrips are strongly inhomogeneous [2]. While it is possible to derive an approximate analytic expression for the general demagnetizing factors of rectangular strips [18], this does not provide information on the actual spatial distribution of the demagnetizing field in each sample orientation and, additionally, does not take into account edge effects [19]. Micromagnetic simulations, on the other hand, together with spatially resolved imaging can provide access to such kind of information for the investigation of SW dynamics in rectangular microelements [14], [20]. In confined structures under uniform excitation, only SW eigenmodes with an odd number of antinodes (amplitude maxima) are expected to occur. This results in a symmetric interference pattern. Changes in the design of the structure, such as the presence of an additional rectangular microstrip, can cause change in the internal field configuration and, therefore, symmetry breaking [7], [21]. In this work, the asymmetry quantification of SW dynamics in confined rectangular microstrips by an asymmetry parameter (AP) is suggested and applied to TR-STXM results and micromagnetic simulations.

Manuscript received 28 March 2023; revised 16 June 2023; accepted 26 June 2023. Date of publication 7 July 2023; date of current version 24 October 2023. Corresponding author: S. Pile (e-mail: santa.pile@jku.at).

Color versions of one or more figures in this article are available at https://doi.org/10.1109/TMAG.2023.3292746.

Digital Object Identifier 10.1109/TMAG.2023.3292746

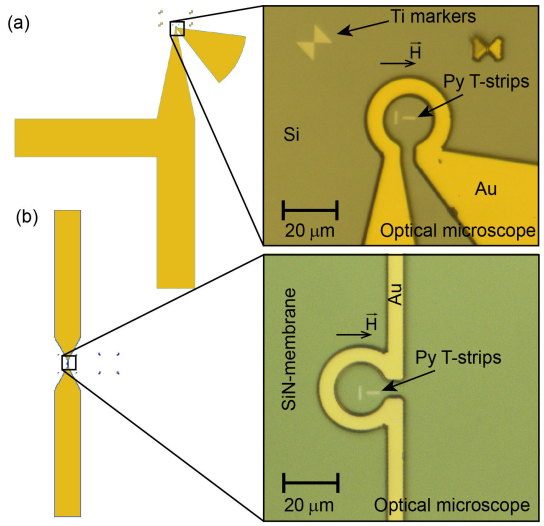

Fig. 1. Schematics of (a) planar microresonator and (b) planar microantenna designs with close-up optical images of the loops with the T-strips inside. The direction of the external static magnetic field ($\vec{H}$) is indicated.

II. Experimental Details

A 30 nm-thick $Ni_{80}Fe_{20}$ (permalloy, Py) single strip [Fig. 2(a) and (b)] and double strips [T-strips, see Figs. 1 and 2(c)] with a nominal rectangular size of 5 × 1 μm^2 were fabricated on different kinds of substrates depending on the measurements as described in more detail in [9]. The scanning electron microscope (SEM) image of the resulting basic rectangular Py microstrip is shown in Fig. 2(a). The nominal distance between the T-strips is 2 μm. The designs of the microresonator used for the FMR measurements and the microantenna used for the TR-STXM measurements are shown in Fig. 1(a) and (b), respectively. Microresonators/microantennas' fabrication details can as well be found in [9].

The microresonator FMR measurements were carried out in a home-built MW spectrometer with field modulation at 78 kHz using a lock-in technique in the field-sweep mode [22], [23], [24]. In the microresonator, the MW field is oriented perpendicular to the sample plane. The external static magnetic field $\vec{H}$ was applied in the plane of the microstrip. In this geometry, during resonance, the dynamic component of the precessing magnetization is oriented out-of-plane. For the FMR measurements, the frequency was fixed to f_{MW} = 14.015 GHz, while sweeping the external static magnetic field from −15 to 600 mT for recording the FMR spectrum.

The TR-STXM experiments were performed at the MAXYMUS endstation of the UE46 undulator beamline at the Helmholtz-Zentrum Berlin during the low-alpha operation mode of the BESSY II synchrotron. For the TR-STXM measurements, the sample is scanned through the focused X-ray beam, while the respective X-ray transmission at each focused point is detected [12]. The sample was scanned in steps of 50 nm. For sensing the dynamic out-of-plane magnetization component $m_z(t)$ at each scan point, the sample was probed perpendicular to its surface. The sample was scanned in steps of 50 nm. The photon energy was tuned to the Fe L_3-edge (∼708 eV). During the TR-STXM measurements, a static magnetic field in the range of 65–120 mT and a small MW field of ∼0.5 mT were applied along the same axis as for the microresonator FMR measurements. The pump-and-probe measurement scheme allows for probing $m_z(t)$ at several intermediate points of the precession. The MW frequency of f_{MW} = 9.43 GHz is phase-locked to the synchrotron frequency, i.e., the frequency of the X-ray flashes impinging on the sample [9], [25]. Hence, TR-STXM images of $m_z(t)$ dynamics were taken at seventh points per excitation period.

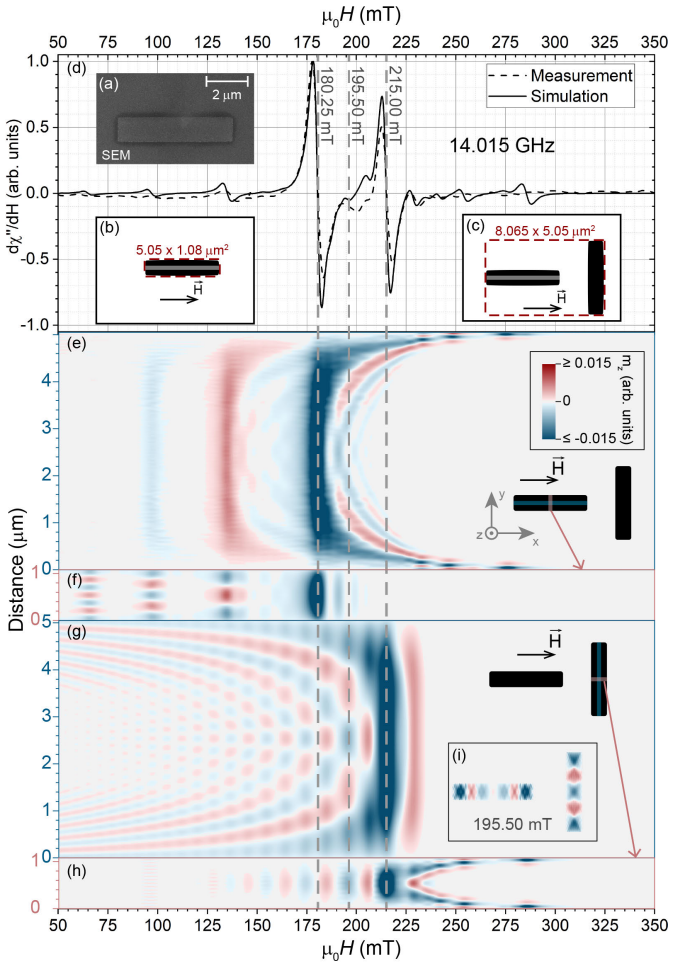

Fig. 2. (a) Scanning electron microscopy image of a single Py microstrip. (b) and (c) Single-strip and T-strip geometries with their lateral sizes as used for the micromagnetic simulations. The direction of the external static magnetic field is indicated. (d) Simulated (solid) and measured (dashed) FMR spectra of the Py T-strips at 14.015 GHz. Overview of the SW profiles (e) and (g) along and (f) and (h) across a strip in (e) and (f) e.a. and (g) and (h) h.a. orientations. (i) Example of the SW patterns at 195.5 mT.

III. Results

A. FMR Versus Micromagnetic Simulations

In Fig. 2(d), the results of the microresonator FMR measurements at f_{MW} = 14.015 GHz are shown as dashed black line for the Py T-strips. The direction of the external static magnetic field is indicated by an arrow in Fig. 2(c). In the FMR spectrum, one can observe two main resonances with large intensities and several other smaller signals above and below the two main signals. The position of the main FMR resonances and their linewidth were used to fit the

measurement results with the simulated FMR spectra [9]. The resulting simulation parameters for the FMR spectrum shown in Fig. 2(d) as a solid black line are: cell size of $8 \times 10 \times 7$ nm^3; sample thickness of 27 nm; no crystalline anisotropy; Py exchange stiffness of 13 pJ/m [26]; saturation magnetization of 750 kA/m; Gilbert damping parameter 0.008; static magnetic field ranging from 400 to 50 mT; and MW frequency of the uniform out-of-plane field of 14.015 GHz [9], [14] with an amplitude of 0.5 mT. The sample designs used for the micromagnetic simulations are shown in Fig. 2(b) and (c). The red dashed frames in the figure mark the simulated areas. The lateral sizes are indicated as well.

Apart from the FMR spectra, simulations provide an additional information about the spatial distribution of the magnetization. The out-of plane component $m_z(t)$ reflects the SW dynamics in the microstrips. In Fig. 2(e)–(h), overviews of the simulated $m_z(t)$ profiles are plotted using the same principle as described in [9]. The overviews display SW profiles along the length [see Fig. 2(e) and (g)] and the width [see Fig. 2(f) and (h)] of each of the T-strips, in easy axis (e.a., external field parallel to the longer edge of the strip) [see Fig. 2(e) and (f)] and in hard axis (h.a., external field parallel to the shorter edge of the strip) [see Fig. 2(g) and (h)] orientation, over a range of external field values in correlation with the FMR spectra in Fig. 2(d). According to the micromagnetic simulations, the main resonance lines at 180.5 and 215.3 mT in Fig. 2(d) correspond to the quasi-uniform FMR excitations. The quasi-uniform mode is the one with almost all the magnetic moments across the strip area precessing in phase with the same opening angle. The reason for the nonuniform $m_z(t)$ spatial distribution closer to the edges [9] is the inhomogeneity of the effective field within the strip. The less pronounced FMR lines correspond to SW excitations with varying amounts of amplitude maxima in their interference pattern [7], [9], [21]. An example of an SW pattern at 195.5 mT is shown in Fig. 2(i), and the corresponding SW profiles are marked with the vertical gray line across Fig. 2(d)–(h). The differences in the resonance fields between the measurement and the simulations at higher fields above 230 mT can possibly stem from the quality of the edges, i.e., the presence of defects etc., which shifts the resonance fields of the localized modes to lower values [9], [19].

For the analysis of the TR-STXM results, all the parameters of the micromagnetic simulations were kept the same, excluding the MW frequency, which was set to $f_{MW} = 9.43$ GHz as used in the measurements. At each field value, the system was excited for 50 MW periods, first 49 of which were skipped as the settling time, and for the last period the spatial distribution of the magnetization was saved in 14 equidistant time frames for further analysis of the spatial maps of $m_z(t)$, which included fast Fourier transform (FFT) analysis similar to that performed on the measured data.

B. TR-STXM and Data Analysis

As described in Section II, the TR-STXM results consist of seven phase images at each static magnetic field value. Each of it contains the spatially distributed counted X-ray photon

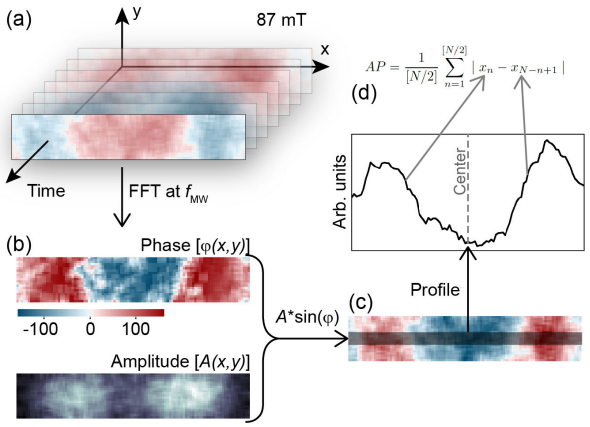

Fig. 3. Schematic representation of the data processing cycle up to AP value calculation. (a) Set of TR-STXM scans at 87 mT. (b) Spatial distribution of the phase and amplitude obtained from the FFT analysis at f_{MW}. (c) SW pattern. (d) SW profile and AP value calculation.

signal corresponding to a certain excitation phase over one MW excitation period and, thus, the magnetization precession cycle [14], [27]. Each scan includes the Py microstrip and a part of the membrane for the background correction. In general, the raw data include a static component corresponding to the chemical contrast of the scanned area and the dynamic component corresponding to the magnetic contrast. For each scanned point in space, the magnetic part was extracted by dividing the counted X-ray photon signal at each time point by the time averaged value over all the time points [14], [25], [28], [29]. Furthermore, a background correction was performed as described in [30]. Upon that, the background part of each scan was removed to proceed only with the data from the Py microstructure. Eventually, the data were filtered in two steps to reduce noise. The first step was an FFT filtering at each point in space by converting the signal from the time to frequency domain, filtering out all the frequencies except for f_{MW}, and converting it back to the time domain via inverse FFT. In the second step, the data were filtered in space by replacing every value by the mean value in its range-2 neighborhood.

For both, the simulated and processed TR-STXM data, a temporal FFT at each point of the spatial distribution of the magnetization was performed to extract the spatial amplitude and phase distribution at the given MW frequency [27], [31] as depicted in Fig. 3(a) and (b). The extracted amplitude and the phase data were combined into a spatial eigenmodes' interference pattern [21] by multiplying the amplitude data with the sine of the phase data as shown in Fig. 3(b) and (c). From the resulting data, the central interference pattern profiles ($m_z(t)$ profiles) were calculated by averaging the central region of the data as shown in Fig. 3(c) and (d). The overviews of the profiles over the range of external static magnetic field were used further to correct the field offset between the simulations and measurements as described in [9].

To quantify symmetry breaking of the SW patterns, an AP is introduced. It indicates a deviation of the SW pattern from the mirror-symmetric state by analyzing its profile (see Fig. 3). A mirror-symmetric profile here means that the profile is

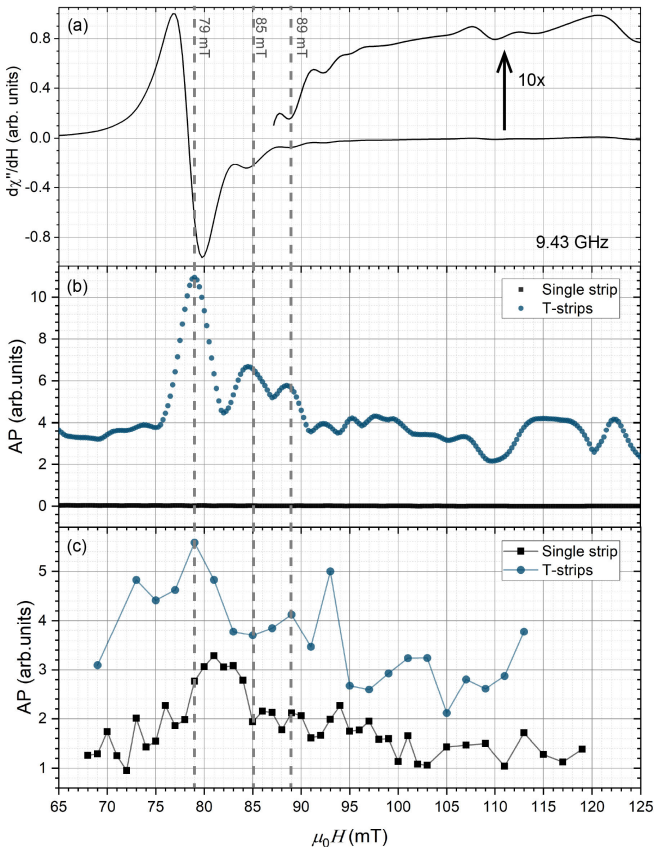

Fig. 4. (a) Simulated FMR spectrum of the Py single strip in e.a. orientation [see Fig. 2(b)]. (b) and (c) AP field dependence calculated from the simulated and measured data, respectively. For strips in e.a. orientation, the corresponding regions of the strips are marked in Fig. 2(a) and (b), respectively.

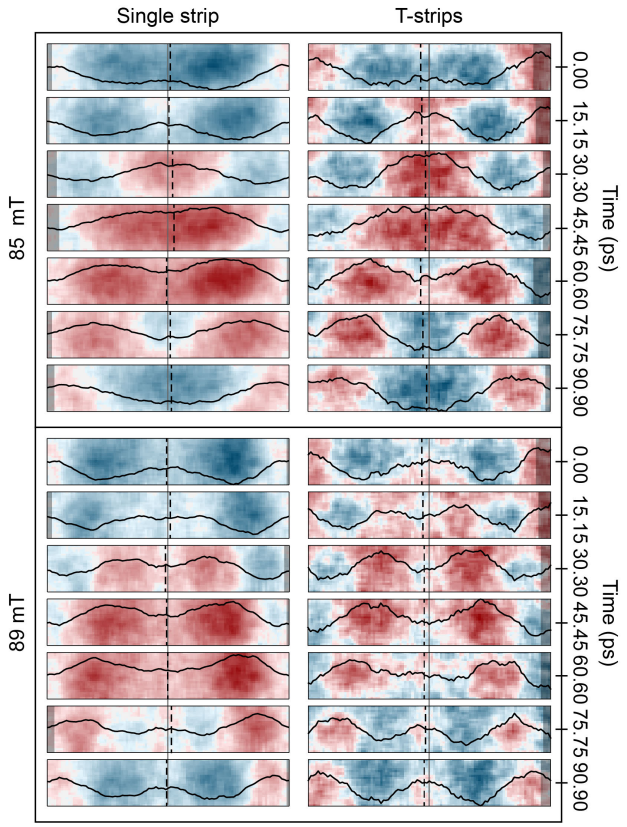

Fig. 5. Measured TR-STXM scans of the SW dynamics at 85 and 89 mT in a strip in e.a. orientation of two sample types: single strip and T-strips. Vertical gray solid lines indicate the physical centers of the strips, while black dashed shorter lines indicate axis of symmetry for each frame. Transparent rectangles correspond to edge shift (see text).

invariant under a reflection about the line in its center (axis of symmetry). The regions of the strips used to calculate the profiles are indicated in Figs. 2(a) and (b) and 3(c) with transparent gray rectangles. The AP for a profile consisting of normalized data values $\{x_n\}_{n=1}^{N}$ is calculated by

$$\mathrm{AP} = \frac{C}{[N/2]} \sum_{n=1}^{[N/2]} | x_n - x_{N-n+1} | \qquad (1)$$

where one half of the profile is subtracted from its other half point by point [see Fig. 3(d)]. Here, C is a scale factor, when comparing different data, the same value is used. Then the mean value of the absolute values of all the differences is taken. Hence, a symmetric profile would give AP = 0.

In Fig. 4(a), a simulated FMR spectrum of the single strip sample in e.a. orientation is shown to correlate the calculated AP values with the FMR positions. The calculated AP values from the simulated and measured data are shown in Fig. 4(b) and (c) for the single-strip and the T-strips samples in e.a. orientation, respectively. Overall, the $m_z(t)$ profiles of the single strip sample appear to be more symmetric compared with the T-strips. This indicates that the SWs in one of the T-strips are affected by the other. Nevertheless, some asymmetry is observed in the single-strip sample in the measured data as well. The reason could be a small tilt of the strip in the scan or sample defects. The first maximum value of the AP is observed at 79 mT, close to the quasi-uniform FMR signal. The second and third maxima are at 84.5 and 88.5 mT, respectively. They are close to the FMR lines corresponding to the SWs with 3 and 5 amplitude maxima [9].

In Fig. 5, the spatial distribution maps of $m_z(t)$ from the TR-STXM scans at 85 and 89 mT of the single-strip and T-strip samples in e.a. orientation are shown. Gray vertical solid lines indicate the physical center of a strip. In addition to the AP value for each phase image shown in Fig. 5, an axis of symmetry was localized, by finding the edge shift of the data array in (1), either left or right, needed to minimize the AP value. The calculated axes of symmetry are indicated with black dashed vertical lines in the figure and the corresponding edge shifts are indicated with transparent rectangles. When looking at the SW dynamics at both the fields, one can see that the $m_z(t)$ patterns are more symmetric with respect to their center for the single strip than for the T-strips. This can be seen even more clearly from the deviation between the physical center and the axes of symmetry in a particular strip. In case of the single strip, the axis of symmetry deviates left and right and the absolute value of deviation ranges from 0 to 0.1 μm. For the T-strips, the axis of symmetry is always shifted left (the opposite side from where the second strip is located [see Fig. 2(c)]) with the absolute values of the deviation ranging from 0.05 to 0.2 μm. The reason for that might be inhomogeneous external static and/or dynamic magnetic stray fields generated by the second strip.

IV. Conclusion

In summary, we gained insight on the SW dynamics in confined rectangular Py microstrips, both single and T-strips, using microresonator FMR measurements, TR-STXM imaging with high spatial and temporal resolution with the support of micromagnetic simulations. To evaluate the sample design influence on the SW behavior, the asymmetries of the SW patterns were analyzed by means of the introduced AP value. The AP value allows for a sensitive quantification of the symmetry breaking of the SW profiles and, therefore, patterns. The results of the measurements and the simulations show a higher SW asymmetry in the T-strips, in particular for the analyzed strip being in e.a. orientation, when compared with a single strip of the same shape and size. This is an indicator of an influence of one strip onto the SW pattern in the other. The reason can be either an inefficient dynamic coupling between the strips [32] or/and the mutual static stray field that changes the effective field distribution within the strips.

Acknowledgment

The authors would like to thank Helmholtz-Zentrum Berlin for the allocation of synchrotron radiation beamtime. They also would like to thank T. Feggeler and H. Stoll for their help during the TR-STXM measurements and A. Halilovic for valuable contributions to the lithography process. In addition, they also would like to thank M. Bechtel for technical support at the beamline. This research was funded in part by the Austrian Science Fund (FWF) under Project ESP 4 ESPRIT-Program and under Project I-3050 during early stage of the work. For the purpose of open access, the authors have applied a CC BY public copyright licence to any Author Accepted Manuscript version arising from this submission. The work of Sina Mayr was supported by the Swiss National Science Foundation (SNSF) under Grant 172517.

References

[1] A. V. Chumak et al., "Advances in magnetics roadmap on spin-wave computing," *IEEE Trans. Magn.*, vol. 58, no. 6, pp. 1–72, Jun. 2022.

[2] C. Bayer et al., "Spin-wave excitations in finite rectangular elements of $Ni_{80}Fe_{20}$," *Phys. Rev. B, Condens. Matter*, vol. 72, Aug. 2005, Art. no. 064427.

[3] T. Sebastian, K. Schultheiss, B. Obry, B. Hillebrands, and H. Schultheiss, "Micro-focused Brillouin light scattering: Imaging spin waves at the nanoscale," *Front. Phys.*, vol. 3, p. 35, Jun. 2015.

[4] Z. Duan, I. N. Krivorotov, R. E. Arias, N. Reckers, S. Stienen, and J. Lindner, "Spin wave eigenmodes in transversely magnetized thin film ferromagnetic wires," *Phys. Rev. B, Condens. Matter*, vol. 92, no. 10, Sep. 2015, Art. no. 104424.

[5] T. Brächer, P. Pirro, and B. Hillebrands, "Parallel pumping for magnon spintronics: Amplification and manipulation of magnon spin currents on the micron-scale," *Phys. Rep.*, vol. 699, pp. 1–34, Jun. 2017.

[6] M. Vogel, R. Aßmann, P. Pirro, A. V. Chumak, B. Hillebrands, and G. von Freymann, "Control of spin-wave propagation using magnetisation gradients," *Sci. Rep.*, vol. 8, no. 1, Jul. 2018, Art. no. 11099.

[7] P. Clausen et al., "Mode conversion by symmetry breaking of propagating spin waves," *Appl. Phys. Lett.*, vol. 99, no. 16, Oct. 2011, Art. no. 162505.

[8] A. V. Sadovnikov et al., "Magnonic beam splitter: The building block of parallel magnonic circuitry," *Appl. Phys. Lett.*, vol. 106, no. 19, May 2015, Art. no. 192406.

[9] S. Pile et al., "Nonstationary spin waves in a single rectangular permalloy microstrip under uniform magnetic excitation," *Phys. Rev. B, Condens. Matter*, vol. 105, no. 9, Mar. 2022, Art. no. 094415.

[10] A. Banholzer et al., "Visualization of spin dynamics in single nanosized magnetic elements," *Nanotechnology*, vol. 22, no. 29, Jul. 2011, Art. no. 295713.

[11] R. Narkowicz, D. Suter, and R. Stonies, "Planar microresonators for EPR experiments," *J. Magn. Reson.*, vol. 175, no. 2, pp. 275–284, Aug. 2005.

[12] M. Weigand et al., "TimeMaxyne: A shot-noise limited, time-resolved pump-and-probe acquisition system capable of 50 GHz frequencies for synchrotron-based X-ray microscopy," *Crystals*, vol. 12, no. 8, p. 1029, Jul. 2022.

[13] H. Stoll et al., "Imaging spin dynamics on the nanoscale using X-ray microscopy," *Front. Phys.*, vol. 3, p. 26, Apr. 2015.

[14] S. Pile et al., "Non-standing spin-waves in confined micrometer-sized ferromagnetic structures under uniform excitation," *Appl. Phys. Lett.*, vol. 116, no. 7, Feb. 2020, Art. no. 072401.

[15] V. E. Demidov, U.-H. Hansen, and S. O. Demokritov, "Spin-wave eigenmodes of a saturated magnetic square at different precession angles," *Phys. Rev. Lett.*, vol. 98, no. 15, Apr. 2007, Art. no. 157203.

[16] C. Kittel, "On the theory of ferromagnetic resonance absorption," *Phys. Rev.*, vol. 73, no. 2, pp. 155–161, Jan. 1948.

[17] L. R. Walker, "Magnetostatic modes in ferromagnetic resonance," *Phys. Rev.*, vol. 105, p. 309, Jan. 1957.

[18] A. Aharoni, "Demagnetizing factors for rectangular ferromagnetic prisms," *J. Appl. Phys.*, vol. 83, no. 6, pp. 3432–3434, Mar. 1998.

[19] R. D. Mcmichael and B. B. Maranville, "Edge saturation fields and dynamic edge modes in ideal and nonideal magnetic film edges," *Phys. Rev. B, Condens. Matter*, vol. 74, no. 2, Jul. 2006, Art. no. 024424.

[20] C. Abert, "Micromagnetics and spintronics: Models and numerical methods," *Eur. Phys. J. B*, vol. 92, no. 6, p. 92, Jun. 2019.

[21] Z. Zhang et al., "Controlled interconversion of quantized spin wave modes via local magnetic fields," *Phys. Rev. B, Condens. Matter*, vol. 100, no. 1, Jul. 2019, Art. no. 014429.

[22] J. Lumetzberger et al., "Influence of structure and cation distribution on magnetic anisotropy and damping in Zn/Al doped nickel ferrites," *Phys. Rev. B, Condens. Matter*, vol. 102, no. 5, Aug. 2020, Art. no. 054402.

[23] H. Cansever et al., "Investigating spin-transfer torques induced by thermal gradients in magnetic tunnel junctions by using micro-cavity ferromagnetic resonance," *J. Phys. D, Appl. Phys.*, vol. 51, no. 22, Jun. 2018, Art. no. 224009.

[24] H. Cansever and J. Lindner, "Microresonators and microantennas—Tools to explore magnetization dynamics in single nanostructures," *Magnetochemistry*, vol. 7, no. 2, p. 28, Feb. 2021.

[25] M. Weigand, *Realization of a New Magnetic Scanning X-ray Microscope and Investigation of Landau Structures Under Pulsed Field Excitation*. Göttingen, Germany: Cuvillier Verlag, 2015.

[26] A. Vansteenkiste, J. Leliaert, M. Dvornik, M. Helsen, F. Garcia-Sanchez, and B. Van Waeyenberge, "The design and verification of MuMax3," *AIP Adv.*, vol. 4, no. 10, Oct. 2014, Art. no. 107133.

[27] F. Groß, N. Träger, J. Förster, M. Weigand, G. Schütz, and J. Gräfe, "Nanoscale detection of spin wave deflection angles in permalloy," *Appl. Phys. Lett.*, vol. 114, no. 1, Jan. 2019, Art. no. 012406.

[28] S. Bonetti et al., "Microwave soft X-ray microscopy for nanoscale magnetization dynamics in the 5–10 GHz frequency range," *Rev. Sci. Instrum.*, vol. 86, no. 9, Sep. 2015, Art. no. 093703.

[29] S. Pile et al., "Direct imaging of the AC component of pumped spin polarization with element specificity," *Phys. Rev. Appl.*, vol. 14, no. 3, Sep. 2020, Art. no. 034005.

[30] T. Schaffers et al., "Extracting the dynamic magnetic contrast in time-resolved X-ray transmission microscopy," *Nanomaterials*, vol. 9, no. 7, p. 940, Jun. 2019.

[31] B. Zingsem et al., "Evaluation protocol for revealing magnonic contrast in STXM-FMR measurements," 2019, *arXiv:1901.10595*.

[32] A. V. Sadovnikov, E. N. Beginin, S. E. Sheshukova, D. V. Romanenko, Y. P. Sharaevskii, and S. A. Nikitov, "Directional multimode coupler for planar magnonics: Side-coupled magnetic stripes," *Appl. Phys. Lett.*, vol. 107, no. 20, Nov. 2015, Art. no. 202405.